ATTRIBUTES OBFUSCATION WITH COMPLEX-VALUED FEATURES

Anonymous authors
Paper under double-blind review

ABSTRACT

The paper studies the possibility of hiding sensitive input information from the intermediate-layer features without too much accuracy degradation. We propose a generic method to revise a conventional neural network to boost the challenge of adversarially inferring about the input but still yields useful outputs. In particular, the method transforms real-valued features into complex-valued ones, in which the input information is hidden in a randomized phase of the transformed features. The knowledge of the phase acts like a key, with which any party can easily recover the prediction from the processing result, but without which the party can neither recover the output nor distinguish the original input. Preliminary experiments on various datasets and network structures have shown that our method significantly diminishes the adversary's ability in inferring about the input while largely preserves the accuracy of the predicted outcome.

1 INTRODUCTION

Deep neural networks (DNNs) have shown superb capabilities to process massive volume of data, and local devices such as mobile phones, medical equipment, Internet of Things (IoT) devices have become major data entry points in recent years. Although on-device machine learning has exhibited various advantages, it usually burdens thin devices with overwhelming computational overhead. Yet offloading raw data to the cloud would put the individual privacy at risk. Hence a trade-off solution is to offload intermediate features, rather than the raw data, to the cloud for further processing.

However, as shown in the previous literature Dosovitskiy & Brox (2016); Zeiler & Fergus (2014); Mahendran & Vedaldi (2015); Shokri et al. (2017); Ganju et al. (2018); Melis et al. (2019), intermediate-layer features face many privacy threats, where the adversary either reconstructs the input or infers unintended properties about the input. Hence, on-device processing encounters a dilemma, *i.e.* while we expect intermediate-layer features to yield high accuracy, we certainly would not want sensitive information to be leaked.

Therefore, we propose a novel method which tweaks a conventional neural network into a complex-valued one, such that intermediate-layer features are released without sacrificing input privacy too much. The network is termed a complex-valued neural network, because the network has complex-valued features, rather than real-valued features. More precisely, we turn the original real-valued features into complex-valued ones, rotate these features by a random angle, and feed them to the cloud for further processing.

We face two significant challenges in the design. First, the tweaked features have to be correctly handled by the DNN on the cloud. Although network structures vary depending on the input types, it is desired that the piecewise linearity of features is preserved, so that the resulting accuracy does not degrade too much compared with the original features. Second, an adversary who intercepts the features in the middle should not be able to recover the exact input, nor can it reconstruct the correct output. Moreover, the neural network is also supposed to be trained using the original data without additional human supervision and be able to conduct efficient inference.

To overcome the first challenge, we tailor operations of DNN to make the succeeding computation at the cloud invariant to feature rotations, *i.e.,* the DNN can correctly handle the feature and preserve the rotated angle in the output. For the second issue, we adopt generative adversarial networks (GAN) to generate synthesized features to hide the original features. It guarantees k-*anonymity* such that, when

an adversary tries to recover the original input from the complex-valued features, it would recover at least $k-1$ other inputs (Please see Appendix B for detailed discussion). Each of the k reconstructed inputs has equivalent probabilities of being the original input to the attacker. Apart from the GAN part, the training of the neural network has little additional computation overhead and requires no extra denotations.

Contributions of this study can be summarized as follows. We propose to transform conventional DNNs into complex-valued ones, which hide input information into a specific phase. Only the party with the phase information can retrieve the output. Without it, an party can neither recover the input nor the output. Tested on various datasets and DNNs, our method has been shown to yield only moderate computational overhead and little accuracy degradation, while significantly diminishes the adversary's ability.

2 Related Work

Complex-valued neural networks. Using complex-valued features or parameters in neural networks has always been an interesting topic. From the computational perspective, Trabelsi et al. (2018) showed that complex-valued neural networks have a competitive performance with their real-valued counterparts. By augmenting recurrent neural networks with associative memory based on complex-valued vectors, Danihelka et al. (2016) achieved faster learning on memorization tasks. Complex-valued features can contain information in both the phase and the magnitude. An example is that Reichert & Serre (2013) used the phase to indicate properties of spike timing in cortical information processing. We take advantage of the complex-valued feature such that the original features can be hidden in a certain phase.

Privacy-preserving deep learning. Various privacy-preserving mechanisms have been proposed using different definitions of privacy: Osia et al. (2017) applied the Siamese architecture to separate the primary and private information so that the primary information was preserved in the feature. PrivyNet by Li et al. (2017) was proposed to decide the local DNN structure under the privacy constraint based on the peak signal-to-noise ratio or the pixel-wise Euclidean distance. Data nullification and random noise addition were introduced by Wang et al. (2018) to protect private information in the features, which guaranteed differential privacy.

Cryptographic tools have been used to learn from sensitive data. Zhang et al. (2016) adopted homomorphic encryption, in particular, BGV encryption, to encrypt the private data and perform the high-order back-propagation on the encrypted data; Mohassel & Zhang (2017) distributed the private data among two non-colluding servers who performed the secure two-party computation to train models on the joint data. Our scheme achieves *k-anonymity* privacy guarantee such that any adversary can at best reconstruct a number of synthetic inputs from the transformed features and thus it cannot distinguish the original input from others.

3 Threat Model and Privacy Guarantee

In this section, we briefly introduce the threat model and the privacy guarantee that our scheme aims to achieve.

Threat model. In our model, a user processes its raw data locally and transmits the neural network features to the cloud for further processing. An adversary would intercept the transferred features and perform either *feature inversion attacks* or *property inference attacks* on these features to either reconstruct inputs, or infer unintended information. Typical examples of the former attacks include feature inversion by Dosovitskiy & Brox (2016), gradient-based visualization by Zeiler & Fergus (2014); Mahendran & Vedaldi (2015), etc. And the latter ones include membership inference attack by Shokri et al. (2017), passive property inference attack by Ganju et al. (2018) as well as feature leakage in collaborative learning by Melis et al. (2019).

k-anonymity. We aim to achieve the following privacy guarantee: given a transformed feature, an adversary can at best recover a number of features which contain at least another $k-1$ features which are different but cannot be distinguished from the real feature.

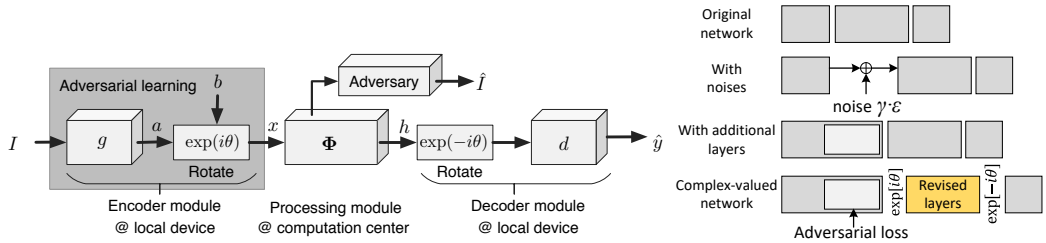

(a) Structure of the complex-valued neural network. (b) Network structures in experiments.

Figure 1: Design overview and network structures under investigation.

4 Approach

4.1 Overview

To fight against the above threats, we propose to revise the conventional DNN. The new structure is shown in Fig. 1a, where the entire network is divided into the following three modules.

- **Encoder** is embedded inside a local device at the user end. The encoder extracts feature from the input, hides true feature by rotating the features by a randomized angle, and sends the encoded result to the cloud.
- **Processing module** is located at the public cloud. This module receives and processes the encoded features without knowing the rotation. At the end of processing, the cloud returns the output to the user.
- **Decoder** is located on the local device of a user. The decoder receives and decodes results sent from the cloud to obtain the final result.

The three modules are jointly trained. Once trained, the encoder and decoder are placed at the local device, whereas the processing module resides on the cloud for public use. We will illustrate the detail of each module in the following section.

4.2 Complex-Valued Neural Networks

Let $(I, y) \in \mathcal{D}$ denote an input and its label in the training dataset and g be the encoder at the local device. Given the input I, the intermediate-layer feature is computed as

$$a = g(I), \tag{1}$$

but we do not directly submit a to the cloud. Instead, we introduce a fooling counterpart b to construct a complex-valued feature as follows:

$$x = \exp(i\theta)\big[a + bi\big], \tag{2}$$

where θ and b are randomly chosen. b is the fooling counterpart which does not contain any private information of a. The encoded feature is then sent to the processing module $\mathbf{\Phi}$, which produces the complex-valued feature $h = \mathbf{\Phi}(x)$. Upon receiving h, the decoder makes prediction $\hat{y}$ on I by inverting the complex-valued feature h back:

$$\hat{y} = d(\Re[h \cdot \exp(-i\theta)]), \tag{3}$$

where d denotes the decoder module, which can be constructed as either a shallow network or just a softmax layer. $\Re(\cdot)$ denotes the operation of picking real parts of complex values.

Processing Module $\mathbf{\Phi}$. The core design of the processing module is to allow the complex-valued feature $h = \mathbf{\Phi}(x)$ to be successfully decoded later by the decoder. *I.e.* if we rotate the complex-valued feature $a + bi$ by an angle θ, all the features of the following layers are supposed to be rotated by the same angle. We represent the processing module as cascaded functions of multiple layers $\mathbf{\Phi}(x) = \Phi_n(\Phi_{n-1}(\cdots \Phi_1(x)))$, where $\Phi_j(\cdot)$ denotes the function of the j-th layer and $f_j = \Phi_j(f_{j-1})$ represents the output of the j-th layer. Thus the processing module should have the following property:

$$\mathbf{\Phi}(f^{(\theta)}) = e^{i\theta}\mathbf{\Phi}(f) \quad \text{s.t. } f^{(\theta)} \triangleq e^{i\theta} f, \ \forall \theta \in [0, 2\pi). \tag{4}$$

In other words, the function of each intermediate layer in the processing module should satisfy

$$\Phi_j(f_{j-1}^{(\theta)}) = e^{i\theta}\Phi_j(f_{j-1}) \quad \text{s.t. } f_{j-1}^{(\theta)} \triangleq e^{i\theta} f_{j-1},\ \forall j \in [2, \ldots, n],\ \forall \theta \in [0, 2\pi). \tag{5}$$

to recursively prove Eqn. (4).

Let us consider six most common types of network layers to construct the processing module, *i.e.* the convolutional layer, the ReLU layer, the batch-normalization layer, the average/max pooling layer, the dropout layer, and the skip-connection operation. For the convolutional layer, we remove the bias term and obtain $\text{Conv}(f) = w \otimes f$, which satisfies Eqn. (5). Inspired by Trabelsi et al. (2018), we replace the ReLU with the following non-linear layer:

$$\delta(f_{ijk}) = \frac{\|f_{ijk}\|}{\max\{\|f_{ijk}\|, c\}} \cdot f_{ijk} \tag{6}$$

where f_{ijk} denotes the neural activation at the location (i, j) in the k-th channel of the feature, and c is a positive constant.

Likewise, the batch-normalization operation is replaced by

$$\text{norm}(f_{ijk}^l) = \frac{f_{ijk}^l}{\sqrt{\mathbb{E}_l[\|f_{ijk}^l\|^2]}}, \tag{7}$$

where f^l denotes the complex-valued tensor for the l-th sample in the batch.

For max-pooling layers, we modify the rule such that the feature with the maximum norm in the region is selected, which ensures that max-pooling does not change the phase of its input.

For the dropout layer, we randomly drops out both the real and imaginary parts of complex-valued features. Skip connections can be formulated as $f + \Phi(f)$, where the inner module $\Phi(f)$ recursively satisfies Eqn. (4).

All above six operations satisfy Eqn. (4). Please see supplementary materials for the proof.

GAN-based Encoder. The objective of the encoder is to hide the real feature a of the input I in a certain phase θ of the encoded feature $x = \exp(i\theta)\big[a + bi\big]$. Let $a' = \Re[x\exp(-i\theta')] = \Re[(a + bi)\exp(i\theta - i\theta')] = \Re[(a + bi)\exp(i\Delta\theta)]$ denote a fake feature decoded using a random angle $\theta' \neq \theta$, where $\Delta\theta = \theta - \theta'$. A ideal encoder requires (i) the fake feature a' contains information beyond what the real feature a contains; (ii) a' and a follow the same distribution so that it is difficult to distinguish the real ones. Hence, we train the encoder g with different values of θ's and b's. We use a GAN to distinguish between the real and faked features. Let D denote the discriminator. We train the encoder over the WGAN (Arjovsky et al. (2017)) loss:

$$\begin{aligned}\min_g \max_D L(g, D) &= \mathbb{E}_{I\sim p_{\mathcal{I}}}\Big[D(a) - \mathbb{E}_{\Delta\theta\sim U(0,\pi), b\neq a}\big[D(a')\big]\Big] \\ &= \mathbb{E}_{I\sim p_{\mathcal{I}}}\Big[D(g(I)) - \mathbb{E}_{\Delta\theta\sim U(0,\pi), b\neq g(I)}\big[D\big(\Re[(g(I) + bi)e^{i\Delta\theta}]\big)\big]\Big].\end{aligned} \tag{8}$$

The encoder g generates features to fool the discriminator. Upon convergence, the distribution of a' approximates that of a. Note that the loss is the expectation over uniform-randomly distributed $\theta \in (0, 2\pi)$. Ideally, the expectation in Eqn. (8) should also be taken over all possible $\Delta\theta \neq 0$, and thus when an adversary tries to recover a by randomly rotating an angle, it will generate an infinite number of features following the same distribution as that of a. Empirically, we pick $k - 1$ such $\Delta\theta$'s uniformly over $(0, \pi)$ and iterate through these $k - 1$ values as negative samples in the adversarial learning. The GAN-based encoder is the key to our k-anonymity guarantee such that it ensures the real feature cannot be distinguished from at least $k - 1$ fake features. Please find the end of Appendix B to see the visualization effect of our privacy guarantee.

The overall loss of learning is formulated as follows, which contains the adversarial loss in Eqn. (8) and a loss for the target task:

$$\min_{g,\mathbf{\Phi},d} \max_D \text{ Loss} = \min_{g,\mathbf{\Phi},d}\big[\max_D L(g, D) + L_{\text{task}}(\hat{y}, y)\big], \tag{9}$$

where $L_{\text{task}}(\hat{y}, y)$ represents the loss for the target task.

	Dataset	Classification Error Rates (%)			Reconstruction Errors			
		Original DNN	DNN with additional layers	Complex-Valued DNN	Original DNN	DNN with additional layers	Complex-Valued dec(a^*)	Complex-Valued dec(x)
ResNet-20-α	CIFAR-10	11.56	9.68	10.91	0.0906	0.1225	0.2664	0.2420
ResNet-20-β	CIFAR-10	11.99	9.79	12.28	0.0967	0.1210	0.2424	0.2420
ResNet-32-α	CIFAR-10	11.13	9.67	**10.48**	0.0930	0.1171	0.2569	0.2412
ResNet-32-β	CIFAR-10	10.91	9.40	11.12	0.0959	0.1189	0.2515	0.2425
ResNet-44-α	CIFAR-10	10.67	9.43	11.08	0.0933	0.1109	0.2746	0.2419
ResNet-44-β	CIFAR-10	10.50	10.15	**10.51**	0.0973	0.1210	0.2511	0.2397
ResNet-56-α	CIFAR-10	10.17	9.16	11.53	0.0989	0.1304	0.2804	0.2377
ResNet-56-β	CIFAR-10	10.78	9.04	11.28	0.0907	0.1176	0.2585	0.2358
ResNet-110-α	CIFAR-10	10.19	9.14	11.97	0.0896	0.1079	**0.3081**	**0.2495**
ResNet-110-β	CIFAR-10	10.21	9.36	11.85	0.0932	0.1152	0.2582	0.2414

Table 1: Classification error rates and reconstruction errors measured on different variants of ResNet and CIFAR-10. Additional layers are introduced due to the GAN structure, but are not trained over adversarial loss. Our results show that the revised DNNs have almost the same utility performance as the original ones, but with greater reconstruction loss.

Note that to simplify the implementation, we compute $b = g(I')$ as the feature of a randomly chosen sample $I' \neq I$ where ideally I' has little correlation with I.

In sum, the entire neural network $[g, \mathbf{\Phi}, d]$ is trained with randomized variables θ and b to minimize the loss in Eqn. (9). Once trained, the network $[g, \mathbf{\Phi}, d]$ is fixed and publicly released. At the inference phase, the encoder secretly selects a fooling counterpart b and a rotation angle θ to encode its real feature a. The decoder receives the processed result h from the cloud, and make the final prediction based on Eqn. (3).

4.3 Attacks to Complex-Valued DNNs

We will materialize the attacks described in the threat model in Sec. 3 and make them specific to our proposed complex-valued DNNs.

Feature inversion attacks: The adversary performs two types of attacks. In **inversion attack 1**, the adversary tries to find out the most likely rotated angle $\hat{\theta}$ to revert the feature x and obtain a^*. An adversary learns to use a^* to reconstruct the input $\hat{I} = \text{dec}(a^*)$. Here we define $a^* = \Re[x \exp(-i\hat{\theta})]$ as the most probable feature recovered by the adversary. The adversary, for instance, can build a new discriminator D' to obtain $\hat{\theta} = \max_\theta D'(\Re[x \exp(-i\theta)])$. In **inversion attack 2**, the adversary learns to directly reconstruct the targeted input from the features, *i.e.,* $\hat{I} = \text{dec}(x)$. We show that our adversarial training strategy boosts the difficulty of learning such a decoder. Let g^* and D^* denote the learned encoder and discriminator, respectively. Based on g^*, let us construct the following discriminator $\hat{D}(a') = -\|g^*(I) - g^*(\text{dec}(a'))\|$. The larger $\hat{D}(a')$ indicates the higher similarity with the real input. Because D^* is learned via $D^* = \arg\max_D L(g^*, D)$, we have $L(g^*, D^*) \geq L(g^*, \hat{D})$. The adversarial loss in Eqn. (8) provides an upper bound of $L(g^*, \hat{D})$, and thus restricts the capability of dec$(\cdot)$.

Property inference attacks: By Ganju et al. (2018), 'property' refers to the input attribute, which can be any sensitive information to protect or any attribute not expected to be released with features. For example, given a facial image dataset and an age recognition task, the gender attribute is required to hide in features. By labeling features with properties of the corresponding inputs, the adversary is able to train classifiers on a dataset consisting all the feature-property pairs. Once trained, the classifiers can use intermediate-layer features to infer if the input possesses certain properties.

We consider four attacking strategies. **Inference attack 1:** the adversary uses raw images to train a classifier to predict hidden properties of the input. At the testing phase, the attacker feeds the reconstructed result dec(a^*) from inversion attack 1 to the classifier to predict hidden properties. **Inference attack 2:** the adversary first rotates x's by their respective $\hat{\theta}$ to estimate the most likely feature a^*. The adversary trains and tests the classifier on a^* to predict hidden properties. **Inference attack 3:** the adversary uses the result of inversion attack 1 dec(a^*) to train and test a classifier to predict hidden properties. **Inference attack 4:** the adversary compares a^* against a of training examples to find its k-nearest neighbors (k-NNs) to predict hidden properties.

If a^* contains sufficient information to recover some property, aforementioned attackers would learn the relationship between a^* (or dec(a^*)) and the hidden property. Otherwise, the model would fail.

Figure 2: Left: CelebA images reconstructed from different features. From top down: original input, reconstruction from 'encoder' output of the original DNN, $\text{dec}(a)$, $\text{dec}(a^*)$, $\text{dec}(x)$. Right: CIFAR-10 images reconstructed from different features. From top down: original input, reconstruction from 'encoder' output of the noisy DNN, –, $\text{dec}(a^*)$, $\text{dec}(x)$. Reconstruction has limited resemblance with the input in the last two rows.

Classification Error Rates

	Dataset	Original DNN	DNN with additional layers	Noisy DNN $\gamma = 0.2$	Noisy DNN $\gamma = 0.5$	Noisy DNN $\gamma = 1.0$	Complex-Valued DNN
LeNet	CIFAR-10	19.78	21.52	24.15	27.53	34.43	**17.95**
LeNet	CIFAR-100	51.45	49.85	56.65	67.66	78.82	**49.76**
ResNet-56-α	CIFAR-100	53.26	44.38	57.24	61.31	74.17	**44.37**
ResNet-110-α	CIFAR-100	50.64	44.93	55.19	61.12	71.31	50.94
VGG-16	CUB-200	56.78	63.47	69.20	99.48	99.48	78.50
AlexNet	CelebA	14.17	9.49	–	–	–	15.94

Reconstruction Errors

	Dataset	Original DNN	DNN with additional layers	Noisy DNN $\gamma = 0.2$	Noisy DNN $\gamma = 0.5$	Noisy DNN $\gamma = 1.0$	Complex-Valued DNN $\text{dec}(a^*)$	Complex-Valued DNN $\text{dec}(x)$
LeNet	CIFAR-10	0.0769	0.1208	0.0948	0.1076	0.1274	**0.2405**	**0.2353**
LeNet	CIFAR-100	0.0708	0.1314	0.0950	0.1012	0.1286	**0.2700**	**0.2483**
ResNet-56-α	CIFAR-100	0.0929	0.1029	0.1461	0.1691	0.2017	**0.2593**	**0.2473**
ResNet-110-α	CIFAR-100	0.1050	0.1092	0.1483	0.1690	0.2116	**0.2602**	**0.2419**
VGG-16	CUB-200	0.1285	0.1202	0.1764	0.0972	0.1990	**0.2803**	**0.2100**
AlexNet	CelebA	0.0687	0.1068	–	–	–	**0.3272**	**0.2597**

Table 2: Classification error rates and reconstruction errors on a variety of DNNs and datasets. We compared the results with noisy DNNs with different noise levels. Complex-Valued DNNs have significantly better accuracy performance and higher reconstruction errors than noisy DNNs over all noise levels.

5 Experiments

We revised a variety of classical DNNs to complex-valued DNNs and tested them on different datasets to demonstrate the broad applicability of our method. Without loss of generality, tasks include object classification and face attribute estimation, but do not exclude other tasks on DNNs. We have applied a total of two inversion attacks and four inference attacks to the complex-valued DNNs for testing the privacy performance.

5.1 Implementation Details

Complex-valued DNNs: We constructed complex-valued DNNs based on 8 classical DNNs in total, which included the ResNet-20/32/44/56/110 (He et al. (2016)), the LeNet (LeCun et al. (1998)), the VGG-16 (Simonyan & Zisserman (2015)), and the AlexNet (Krizhevsky et al. (2012)). As shown in Fig. 1a, we divided each original DNN into three modules which were referred to as the encoder/processing module/decoder correspondingly. The structure is given by the top row of Fig. 1b. The bottom row of Fig. 1b gives the architecture of revised DNNs. Given the original DNNs, the encoder/processing/decoder modules were divided as follows. For the residual network, we tested two variants — *ResNet-*α and *ResNet-*β — in the α-variant, the output of the layer before the first 16×16 feature map was fed to the aforementioned GAN, and layers following the first 8×8 feature map constituted the decoder. The β-variant was the same with the α-variant except that the decoder was composed by the last residual block and the layers following it. The processing module of a residual network was modified such that $c = 1$ in $\delta(\cdot)$ for all non-linear layers.

The encoder of the LeNet consisted of the first convolutional layer and the GAN, whereas its decoder only contained the softmax layer. All layers before the last 56×56 feature map of VGG-16 comprised the encoder. The decoder consisted of fully-connected layers and the softmax layer. For the AlexNet, the output of the first three convolutional layers was fed into GAN, and the decoder contained

	Dataset	Original DNN	w/ additional layers	Noisy DNN $\gamma = 0.2$	Noisy DNN $\gamma = 0.5$	Noisy DNN $\gamma = 1.0$	Complex-Valued DNN $dec(a^*)$	Complex-Valued DNN $dec(x)$
LeNet	CIFAR-10	0.16	0.12	0.20	0.20	0.24	**0.82**	**0.92**
LeNet	CIFAR-100	0.16	0.14	0.20	0.64	0.72	**0.80**	**0.92**
ResNet-56-α	CIFAR-100	0.06	0.06	0.08	0.10	0.36	**0.72**	**0.88**
ResNet-110-α	CIFAR-100	0.04	0.12	0.10	0.16	0.36	**0.80**	**0.86**
VGG-16	CUB-200	0.06	0.06	0.08	0.02	0.14	**0.86**	**0.84**
AlexNet	CelebA	0.04	0.24	–	–	–	**0.96**	**1.00**

Table 3: Failure rate of reconstructed images identification. We have five human annotators to recognize the object in mixed groups of images. The results show that most fail to recognize the reconstruction from the revised DNNs.

	Dataset	Average Error
ResNet-20-α	CIFAR-10	0.7890
ResNet-20-β	CIFAR-10	0.7859
ResNet-32-α	CIFAR-10	0.7820
ResNet-32-β	CIFAR-10	0.7843
ResNet-44-α	CIFAR-10	0.8411
ResNet-44-β	CIFAR-10	0.7853
ResNet-56-α	CIFAR-10	0.8088
ResNet-56-β	CIFAR-10	0.8283
ResNet-110-α	CIFAR-10	0.8048
ResNet-110-β	CIFAR-10	0.7818
LeNet	CIFAR-10	0.7884
LeNet	CIFAR-100	0.8046
ResNet-56-α	CIFAR-100	0.7898
ResNet-110-α	CIFAR-100	0.7878
VGG-16	CUB-200	**1.5572**
AlexNet	CelebA	0.8500

Table 4: Average error (absolute value) of the estimated rotation angle θ in radian.

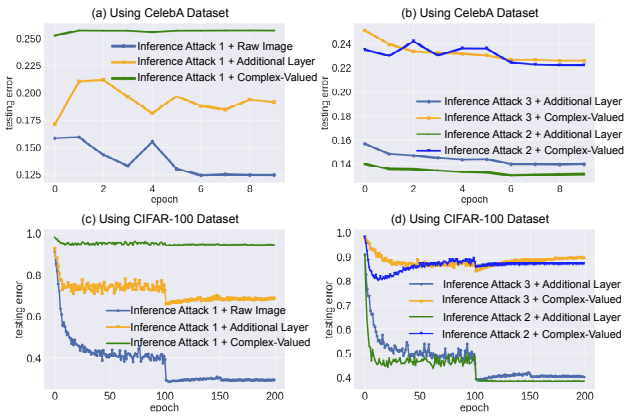

Figure 3: The error rates in inferring hidden properties on CelebA (a)/(b) and CIFAR-100 (c)/(d).

fully-connected layers and the softmax layer. In the processing modules of these DNNs, we set $c_k = \mathbb{E}_{ij}\|x'_{ijk}\|$ for neural activations in the k-th channel.

Baselines: Beside the complex-valued DNN, we constructed three baseline networks for comparison.

Original DNNs (baseline 1): The original DNN without any revision was taken as the first baseline network. For ease of presentation, we also divided the original DNNs into the encoder, the processing module, and the decoder. The division of modules for original DNNs was the same as that for complex-valued DNNs.

Noisy DNNs (baseline 2): Based on the original DNNs, we injected noise right after the encoder module, which was given as $a + \gamma \cdot \epsilon$ (we set $\gamma = 0.5, 1.0, 2.0$). The noisy feature was fed to the processing module instead of a, as shown in the second row of Fig. 1b. Here ϵ represents a high-dimensional random noise with the same average magnitude as a.

DNNs with additional layers (baseline 3): Since the encoder was based on GAN, additional layers needed to be added, when we revised the DNN. We chose a GAN which incorporated a generator consisting of a convolutional layer with $3 \times 3 \times K$ filters, and a discriminator composed by a convolutional layer as well as a fully-connected layer. We designed this baseline for fair comparison, because additional layers in GAN, although without adversarial loss, would incur model structure changes. Its structure is illustrated by the third row of Fig. 1b.

Attacks: Privacy attacking was implemented as follows. (1) *Inversion attacks:* we implemented the inversion attacker based on U-net (Ronneberger et al. (2015)). The original U-net consisted of 8 blocks, and we revised each block to contain six convolutional layers for better reconstruction performance. (2) *Inference attacks:* we selected CelebA and CIFAR-100 datasets to test robustness against property inference attacks. For CelebA, we evaluated the accuracy performance on classifying 30 attributes and the privacy performance on the rest 10 attributes. Likewise, the accuracy of the DNN on CIFAR-100 was evaluated by the classification error of the major 20 superclasses, and the privacy was gauged by the classification error of the 100 minor classes.

CelebA and CIFAR-100 adopted the AlexNet and the ResNet-56, respectively, as prototype models. Their attacker nets were implemented as the ResNet-50 and the ResNet-56, respectively.

		Classification Error Rates	Hidden Properties Error Rates			Speed(s/images)
Dataset	DNN structure		1-NN	3-NN	5-NN	
CelebA	w/ additional layers	0.0804	0.2014	0.1726	0.162	0.0026
CelebA	Complex-Valued DNN	0.1475	**0.3169**	0.2790	0.2641	0.0027
CIFAR-100	w/ additional layers	0.1873	0.7338	0.6837	0.7116	0.0004
CIFAR-100	Complex-Valued DNN	0.2677	**0.9444**	0.9363	0.925	0.0007

Table 5: The classification error rates, error rates in inferring hidden properties by k-NN, and processing speed. We found that while introducing little computational overhead, our method diminishes the adversary's power in inferring hidden properties.

5.2 Evaluation metrics

We evaluated three aspects of the revised DNNs' performance: accuracy, privacy, and efficiency. *Accuracy* concerned the performance of the model on the task. *Privacy* was measured by the robustness of our DNNs against inversion attacks and inference attacks. More specifically, for inversion attacks, we had the following measures: (1) the average error of the estimation about the rotated angle θ^*, *i.e.* $|\theta^* - \hat{\theta}|$; (2) the pixel-level reconstruction error $\mathbb{E}[\|\hat{I} - I\|]$ where the value of each pixel was scaled to $[0, 1]$; (3) failure rate of human identification of the reconstructed images. For inference attacks, we measured the robustness of DNNs by the error rate of each attack model (see Sec. 4.3). As to *efficiency*, we measured the processing time compared with the baseline.

5.3 Experimental Results and Analysis

Fig. 2 visualizes images reconstructed using features of different baseline networks. Due to space constraint, this figure only shows partial results. For a complete result, please refer to the supplementary file. Visual effects were significant as the reconstruction in the bottom two rows greatly shifted away from the original input. Obviously, other misleading input attributes were mixed up with the original ones. To further examine the effect, we compared classification error rates and reconstruction errors on a variety of datasets and DNNs in Table 1 and 2. Since the revised DNNs introduced additional layers to the original DNNs, we compared the performance of both the original DNNs as well as those with additional layers. Our complex-valued DNNs achieved similar utility performance, and exhibited significantly higher reconstruction error in almost all groups.

Further, we mimiced the adversary to recover the rotated angle θ^* with the help of a discriminator model. Most errors fell into $(\pi/4, \pi/2)$ according to Table 4, which indicates even the discriminator could not tell the original features. We also qualitatively tested the reconstructed result in Table 3.

Fig. 3 and Table 5 show the error rates in inferring hidden properties by attackers. We observed that in Fig. 3-(a),(c), the error rate of the inference attack 1 on the complex-valued DNNs (dec(a^*)) was significantly higher than on the baseline 1 (raw images) and baseline 3 (dec(a)), and was close to random selection (99%) on CIFAR-100. We further tested inference attack 2 and 3. In Fig. 3-(b),(d), the error rates of the attacker nets trained on a^* and dec(a^*) were both significantly higher than that of baseline 3, *i.e.* a^* indicated little about the hidden properties. k-NN methods yielded similar results. Last but not least, we compared the running time of processing the images with different DNNs. Batch size of 128 and 100 are used respectively for CelebA and CIFAR-100. It is shown that the complex-valued DNNs had comparable performance with the baseline.

6 Conclusion and Discussions

We propose a novel method to preserve input privacy in the intermediate-layer features. The method transforms a traditional DNN into a complex-valued one to the adversary. Our method has been tested on a variety of datasets and models. Experiments have shown the effectiveness of our method in compromising the adversary's capability while largely preserving accuracy. Please also find in Appendix C the discussion on the potential challenges and limitation of our work.

Theoretically, not only the encoder output but also all other intermediate-layer features in the processing module can preserve privacy. However, we only need to invert the encoder output layer to test the privacy performance, since all features in successive layers can be expressed as functions of that layer. Thus we can roughly consider the performance of the encoder output as the lower bound of other features.

REFERENCES

Martin Abadi, Andy Chu, Ian Goodfellow, H Brendan McMahan, Ilya Mironov, Kunal Talwar, and Li Zhang. Deep Learning with Differential Privacy. In *Proc. of the 2016 ACM SIGSAC Conference on Computer and Communications Security (CCS)*, pp. 308–318. ACM, 2016.

Martin Arjovsky, Soumith Chintala, and Lon Bottou. Wasserstein Generative Adversarial Networks. In *Proceedings of the 34th International Conference on Machine Learning*, pp. 214–223, 2017.

Ivo Danihelka, Greg Wayne, Benigno Uria, Nal Kalchbrenner, and Alex Graves. Associative Long Short-Term Memory. 2016.

Alexey Dosovitskiy and Thomas Brox. Inverting Visual Representations with Convolutional Networks. In *Proc. of the IEEE Conference on Computer Vision and Pattern Recognition (CVPR)*, pp. 4829–4837, 2016.

Karan Ganju, Qi Wang, Wei Yang, Carl A Gunter, and Nikita Borisov. Property inference attacks on fully connected neural networks using permutation invariant representations. In *Proceedings of the 2018 ACM SIGSAC Conference on Computer and Communications Security*, pp. 619–633. ACM, 2018.

Kaiming He, Xiangyu Zhang, Shaoqing Ren, and Jian Sun. Deep residual learning for image recognition. *In CVPR*, 2016.

Alex Krizhevsky, Ilya Sutskever, and Geoffrey E Hinton. Imagenet classification with deep convolutional neural networks. In *Advances in Neural Information Processing Systems (NIPS)*, pp. 1097–1105, 2012.

Y. LeCun, L. Bottou, Y. Bengio, and P. Haffner. Gradient-based learning applied to document recognition. *In Proceedings of the IEEE*, 1998.

Meng Li, Liangzhen Lai, Naveen Suda, Vikas Chandra, and David Z Pan. PrivyNet: A Flexible Framework for Privacy-Preserving Deep Neural Network Training. *arXiv preprint arXiv:1709.06161*, 2017.

Aravindh Mahendran and Andrea Vedaldi. Understanding deep image representations by inverting them. In *Proceedings of the IEEE conference on computer vision and pattern recognition*, pp. 5188–5196, 2015.

Luca Melis, Congzheng Song, Emiliano De Cristofaro, and Vitaly Shmatikov. Exploiting unintended feature leakage in collaborative learning. IEEE, 2019.

Payman Mohassel and Yupeng Zhang. SecureML: A System for Scalable Privacy-Preserving Machine Learning. In *2017 38th IEEE Symposium on Security and Privacy (SP)*, pp. 19–38. IEEE, 2017.

Seyed Ali Osia, Ali Shahin Shamsabadi, Ali Taheri, Kleomenis Katevas, Sina Sajadmanesh, Hamid R Rabiee, Nicholas D Lane, and Hamed Haddadi. A Hybrid Deep Learning Architecture for Privacy-Preserving Mobile Analytics. *arXiv preprint arXiv:1703.02952*, 2017.

David P Reichert and Thomas Serre. Neuronal Synchrony in Complex-Valued Deep Networks. *arXiv preprint arXiv:1312.6115*, 2013.

Olaf Ronneberger, Philipp Fischer, and Thomas Brox. U-net: Convolutional networks for biomedical image segmentation. *In CVPR*, 2015.

Reza Shokri and Vitaly Shmatikov. Privacy-preserving Deep Learning. In *Proc. of the 22nd ACM SIGSAC Conference on Computer and Communications Security (CCS)*, pp. 1310–1321. ACM, 2015.

Reza Shokri, Marco Stronati, Congzheng Song, and Vitaly Shmatikov. Membership inference attacks against machine learning models. In *2017 IEEE Symposium on Security and Privacy (SP)*, pp. 3–18. IEEE, 2017.

Karen Simonyan and Andrew Zisserman. Very deep convolutional networks for large-scale image recognition. *In ICLR*, 2015.

Shuang Song, Kamalika Chaudhuri, and Anand D Sarwate. Stochastic Gradient Descent with Differentially Private Updates. In *Proc. of the 2013 IEEE Global Conference on Signal and Information Processing (GlobalSIP)*, pp. 245–248. IEEE, 2013.

Chiheb Trabelsi, Olexa Bilaniuk, Ying Zhang, Dmitriy Serdyuk, Sandeep Subramanian, João Felipe Santos, Soroush Mehri, Negar Rostamzadeh, Yoshua Bengio, and Christopher J Pal. Deep Complex Networks. 2018.

Ji Wang, Jianguo Zhang, Weidong Bao, Xiaomin Zhu, Bokai Cao, and Philip S Yu. Not Just Privacy: Improving Performance of Private Deep Learning in Mobile Cloud. In *Proc. of the 24th ACM SIGKDD International Conference on Knowledge Discovery & Data Mining*, pp. 2407–2416. ACM, 2018.

Matthew D Zeiler and Rob Fergus. Visualizing and understanding convolutional networks. In *European conference on computer vision*, pp. 818–833. Springer, 2014.

Qingchen Zhang, Laurence T Yang, and Zhikui Chen. Privacy preserving deep computation model on cloud for big data feature learning. *IEEE Transactions on Computers*, 65(5):1351–1362, 2016.

A PROOF OF $\Phi(e^{i\theta}x) = e^{i\theta}\Phi(x)$

In this paper, we design the processing module to ensure features of all layers are rotated by the same angle, in order to enable the later decryption of the feature.

$$\left.\begin{array}{r} x^{(0)} = a + bi \\ x^{(\theta)} = e^{i\theta}x^{(0)} \end{array}\right\} \Rightarrow \forall j,\ f_j^{(\theta)} = e^{i\theta} f_j^{(0)}$$

where $f_j^{(\theta)}$ and $f_j^{(0)}$ represent the feature map computed using the input $x^{(\theta)}$ and that computed using the input $x^{(0)}$, respectively.

In order to prove the above equation, we revise basic layers/operations in the processing module to ensure

$$\Phi(e^{i\theta}x) = e^{i\theta}\Phi(x)$$

where $\Phi(\cdot)$ denotes the function of a certain layer/operation. x is given as the input of the specific layer/operation $\Phi(\cdot)$. Based on this equation, we can recursively prove $f_j^{(\theta)} = e^{i\theta} f_j^{(0)}$.

Let us consider the following six most common types of layers/functions to construct the processing module, *i.e.* the conv-layer, the ReLU layer, the batch-normalization layer, the average/max pooling layer, the dropout layer, and the skip-connection operation.

1. We revise the conv-layer by omitting the bias term. Thus, we get

$$\Phi(e^{i\theta}x) = w \otimes [e^{i\theta}x] = e^{i\theta}[w \otimes x] = e^{i\theta}\Phi(x)$$

2. We replace the ReLU layer with the non-linear activation function of $\phi(x_{ijk}) = \frac{\|x_{ijk}\|}{\max\{\|x_{ijk}\|, c\}} \cdot x_{ijk}$. Thus, we can write the element-wise operation as follows.

$$\phi(e^{i\theta}x_{ijk}) = \frac{\|e^{i\theta}x_{ijk}\|}{\max\{\|e^{i\theta}x_{ijk}\|, c\}} \cdot [e^{i\theta}x_{ijk}] = e^{i\theta}\Big[\frac{\|x_{ijk}\|}{\max\{\|x_{ijk}\|, c\}} \cdot x_{ijk}\Big] = e^{i\theta}\phi(x_{ijk})$$

3. We replace the batch-normalization layer with the function of $\phi(x_{ijk}^l) = \frac{x_{ijk}^l}{\sqrt{\mathbb{E}_{ijl}[\|x_{ijk}^l\|^2]}}$. Thus, we can write the element-wise operation as follows.

$$\phi(e^{i\theta}x_{ijk}^l) = \frac{e^{i\theta}x_{ijk}^l}{\sqrt{\mathbb{E}_{ijl}[\|e^{i\theta}x_{ijk}^l\|^2]}} = e^{i\theta}\Big[\frac{x_{ijk}^l}{\sqrt{\mathbb{E}_{ijl}[\|x_{ijk}^l\|^2]}}\Big] = e^{i\theta}\phi(x_{ijk}^l)$$

4. For the the average/max pooling layer and the dropout layer, we can represent their functions in the form of $\Phi(x) = Ax$, where x is given as a vectorized feature, and A denotes a matrix. For the average/max-pooling operation, A represents the selection of neural activations. For the dropout layer, A contains binary values that indicate the dropout state. In this way, we get

$$\Phi(e^{i\theta}x) = A(e^{i\theta}x) = e^{i\theta}[Ax] = e^{i\theta}\Phi(x)$$

5. For the skip-connection operation, we get

$$\Phi(e^{i\theta}x) = e^{i\theta}x + \Psi(e^{i\theta}x) = e^{i\theta}[x + \Psi(x)] = e^{i\theta}\Phi(x)$$

where $\Psi(\cdot)$ denotes the function that is skipped by the connection. We can recursively ensure $\Psi(e^{i\theta}x) = e^{i\theta}\Psi(x)$.

B EXPERIMENTS: VISUALIZATION

Fig. 4, Fig. 5 and Fig. 6 respectively give the visualization effect on CIFAR-10, CUB200-2011, and CelebA, when reconstructing the inputs from features.

Fig. 7 shows the reconstructed input images when an adversary launches a feature inversion attack: it rotates x by an angle continuously drawn from $(0, 2\pi)$ and then reconstruct the input on the rotated

Figure 4: CIFAR-10 images reconstructed from different features on a variety of LeNet-based neural networks.

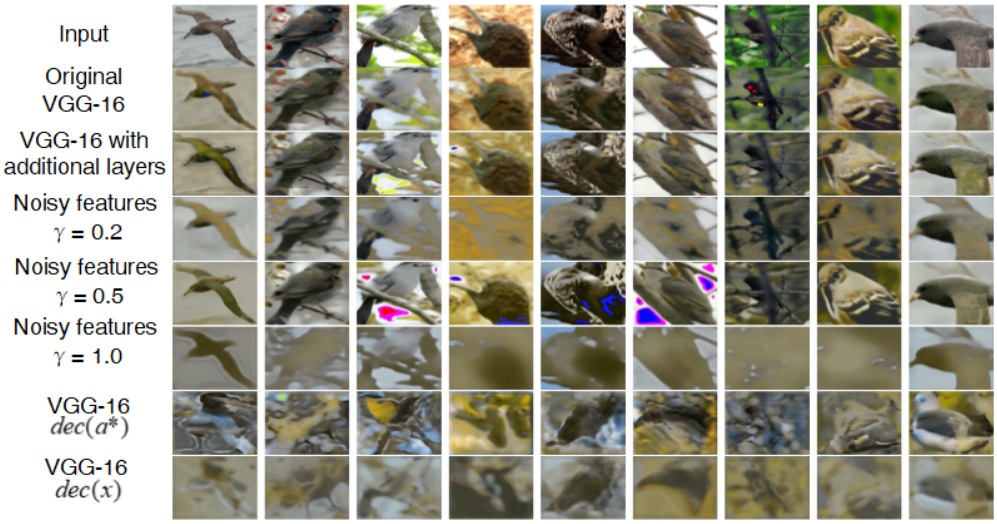

Figure 5: CUB200-2011 images reconstructed from different features on a variety of VGG-16-based neural networks.

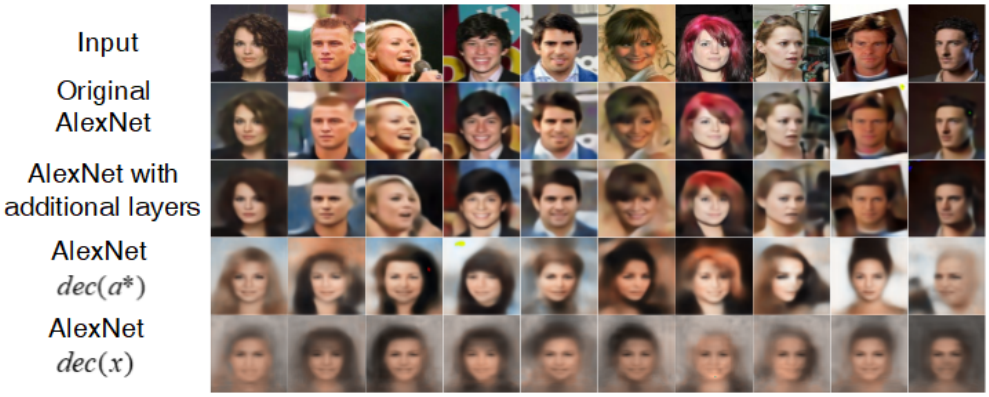

Figure 6: CelebA images reconstructed from different features on a variety of AlexNet-based neural networks.

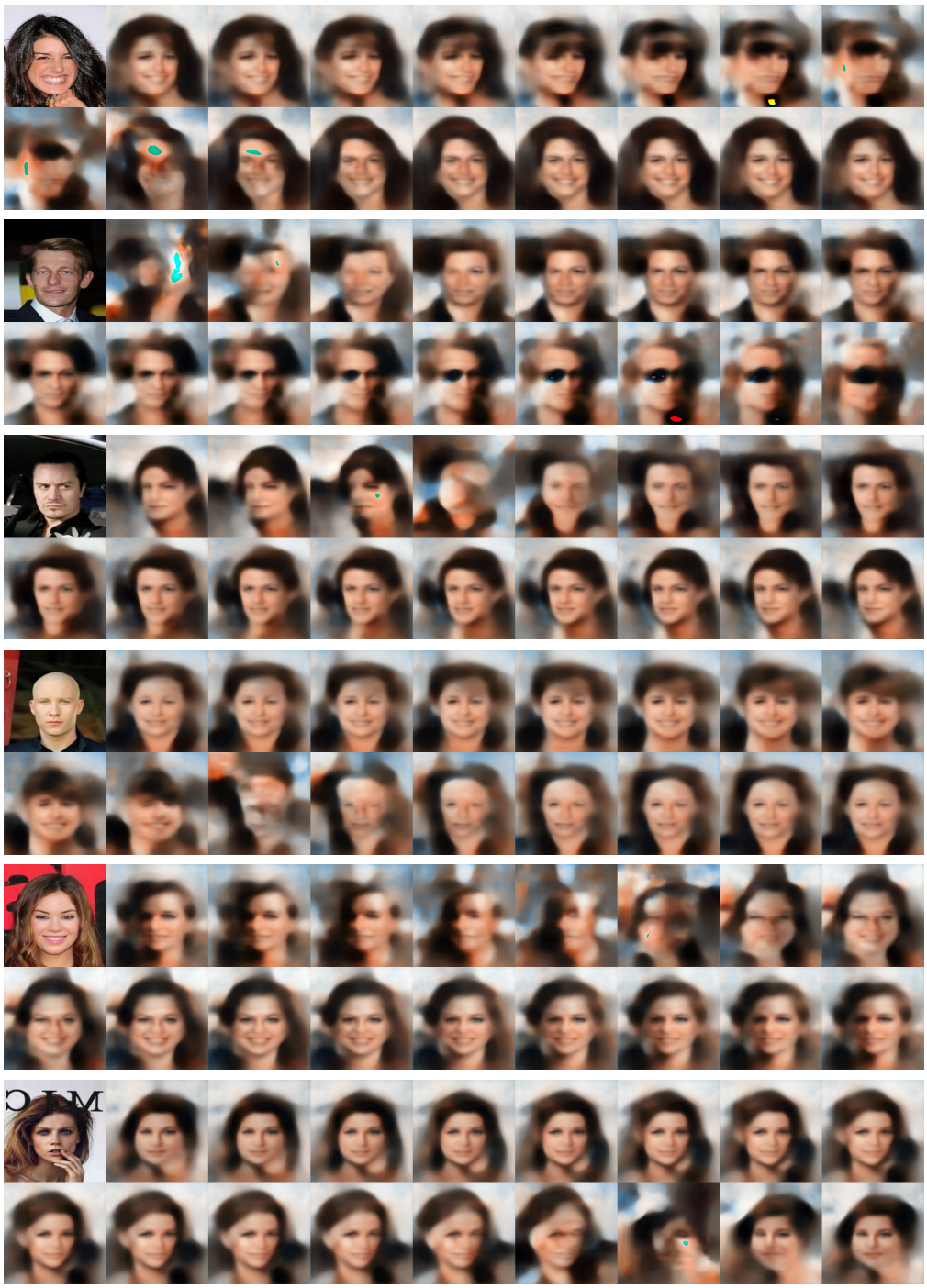

Figure 7: CelebA images reconstructed from feature x rotated by different angles within $(0, 2\pi)$. We pick the most meaningful ones. The first image of every two row is the original input image.

features. The first image of every two row is the original input image. We found that most meaningful reconstructed pictures are mostly drawn from $(\theta + \frac{\pi}{4}, \theta - \frac{3\pi}{4})$. Most reconstructed images have little resemblance to the original input, and present meaningful interpolation of the original sample and the randomly chosen sample. The result is an illustration of our k-anonymity privacy guarantee.

Fig. 8 shows images reconstructed from correctly decoded features. The result demonstrates that, with the 'key' — θ, one can successfully recover original inputs from features.

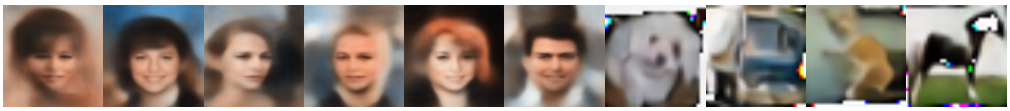

Figure 8: CelebA images and CIFAR-10 images reconstructed from feature x correctly decoded with the knowledge of θ. The reconstructed images have high similarity with the original inputs.

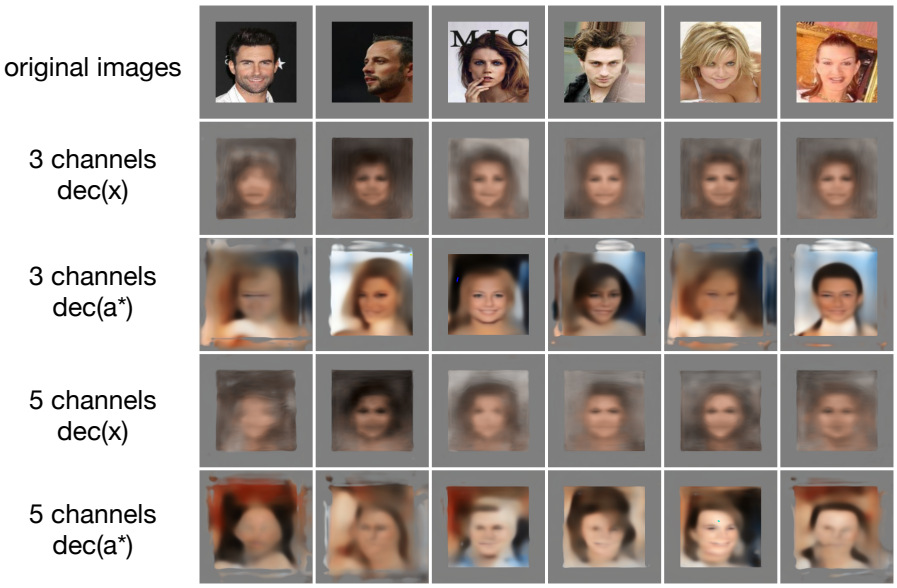

Figure 9: CelebA images reconstructed from features with many zeros. Even if the images are sparse, the adversary cannot recover any useful information from the features.

C Experiments: Attack with Side Information

We consider attacks with side information in this section. As we cannot give a complete list of such side information, we show an example where an adversary launches attacks to features with many zero values to see if it can recover the input. Fig. 9 shows the reconstruction results when the images are sparse with many zeros. The top row of the figure gives the original input where we shrink the CelebA images from $224 \times 224 \times 3$ to $160 \times 160 \times 3$ and pad them to their original size. The second/fourth and third/fifth rows respectively give the reconstruction results of dec(x) and dec(a^*) when the channel number is 3 and 5. As we can tell, even with the side information that the original images are padded with many zeros, it is hard for the adversary to recover images resembling the original inputs.

D Error Distribution of the Estimated Rotation Angle

For a complete view on the error distribution of the estimated rotation angle, we re-display the results of Table 4 in Table 6 and Fig. 10. In Fig. 10, we choose two representative results. The estimated θ on ResNet-44-β is centralized around 300 degree but spreads across a range of 100 degrees. The value on VGG-16 almost spreads across the whole range of $(0, 2\pi)$.

	Dataset	Error Mean	Error STD
ResNet-20-α	CIFAR-10	-0.7887	0.3728
ResNet-20-β	CIFAR-10	-0.7858	0.2944
ResNet-32-α	CIFAR-10	-0.7818	0.3634
ResNet-32-β	CIFAR-10	-0.7842	0.3273
ResNet-44-α	CIFAR-10	-0.7850	0.6897
ResNet-44-β	CIFAR-10	-0.7852	0.3314
ResNet-56-α	CIFAR-10	-0.7851	0.6163
ResNet-56-β	CIFAR-10	-0.7833	0.5998
ResNet-110-α	CIFAR-10	-0.7959	0.4688
ResNet-110-β	CIFAR-10	-0.7813	0.3420
LeNet	CIFAR-10	-0.7833	0.4244
LeNet	CIFAR-100	-0.7776	0.5670
ResNet-56-α	CIFAR-100	-0.7822	0.5650
ResNet-110-α	CIFAR-100	-0.7864	0.3803
VGG-16	CUB-200	-0.1151	1.784
AlexNet	CelebA	-0.7889	0.6617

Table 6: Error distribution of the estimated rotation angle θ in radian.

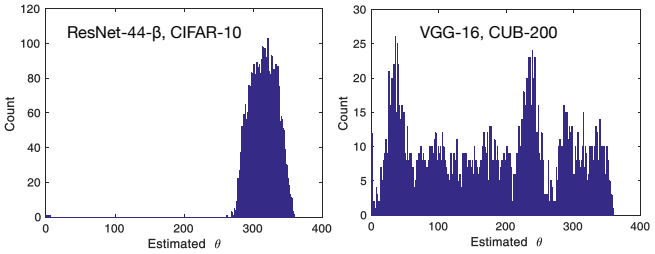

Figure 10: Histogram of the error in estimating the rotation angle θ.

E Feature Distributions

We also conduct an unsupervised explorative analysis of the intermediate-layer feature distributions: Fig. 11-(a) shows the visualization results of features of a conventional ResNet-56 and a complex-valued ResNet-56. Both networks are learned on CIFAR-10. Different colored digits represent different classes. As we can tell, complex-valued features hide categorical information better than its counterparts in conventional neural networks.

F Learning Attribute Correlations

We perform an experiment to test whether or not our complex-valued DNN can prevent the adversary from learning attribute correlations. We learn a traditional ResNet-56 and a complex-valued ResNet-56 to classify major 20 superclasses in the CIFAR-100 dataset. For each trained ResNet-56, let x_I denote the intermediate-layer feature corresponding the image I. For every pair of x_I and $x_{I'}$, we label the pair as correlated if the ground truth of I and I' belong to the same superclass, and uncorrelated otherwise. We train a classifier on such feature-label pairs to see if the classifier can learn such correlation between attributes. The results are shown in Fig. 11-(b), respectively for the original feature and the complex-valued one. The high error (42.41%) of latter illustrates the complex-valued feature preserves the attribute correlations.

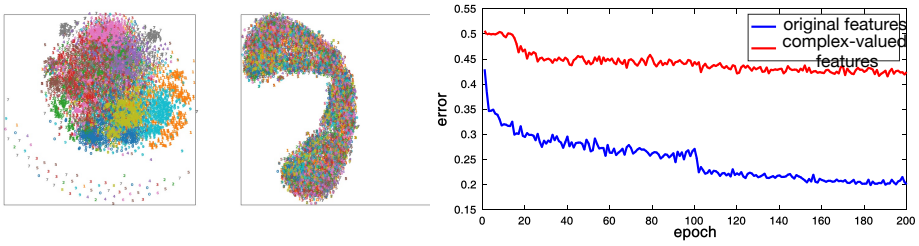

(a) t-SNE visualization of the original and complex-valued features.

(b) Correlation test of the original and complex-valued features.

Figure 11: (a) t-SNE visualization of the original and complex-valued features. (b) Learning attribute correlations from the original and complex-valued features.